Combustion and Flame 179 (2017) 338–353

Contents lists available at ScienceDirect

Combustion and Flame

journal homepage: www.elsevier.com/locate/combustflame

A generalized model of flame to surface heat feedback for laminar wall flames

Isaac T. Leventon, Kevin T. Korver, Stanislav I. Stoliarov*

University of Maryland, Department of Fire Protection Engineering, College Park, MD 20742, United States

ARTICLE INFO

Article history:
Received 16 September 2016
Revised 8 February 2017
Accepted 8 February 2017

Keywords:
Fire dynamics
Flame spread
Vertical burning
Flame heat flux
Heat of combustion
Polymeric fuels

ABSTRACT

In this work, experimental measurements of flame heat flux and sample mass loss rate are obtained as a diffusion flame spreads vertically upward (in the direction opposed to the vector of gravity) over the surface of seven commonly used polymeric materials, two of which are glass reinforced composites. Using these measurements, a previously developed empirical flame model specific to poly(methyl methacrylate) is generalized such that it can predict (flame to material surface) heat feedback from 3 to 20 cm tall flames supported by a wide range of materials. Model generalization is accomplished through scaling on the basis of a material's gaseous pyrolyzate heat of combustion, which can be measured using mg-sized material samples in a microscale combustion calorimeter. For all seven materials tested in this work, which represent diverse chemical compositions and burning behaviors including polymer melt flow, sample burnout, and heavy soot and solid residue formation, model-predicted flame heat flux (to a water-cooled heat flux gauge) is shown to match experimental measurements taken across the full length of the flame with an average absolute error of 3.8 kW m^{-2} (approximately 10–15% of peak measured flame heat flux). Coupled with a numerical pyrolysis solver, this generalized wall flame model provides the framework to quantitatively study material propensity to ignite and support early fire growth in a range of common scenarios with a level of accuracy and reduced computational cost unmatched by other currently available modeling tools.

1. Introduction

Understanding the dynamics of fire inception and growth on organic solids is highly important for engineering fire safety in the built environment. Among organic solids, synthetic polymers and polymer based composites are used increasingly due to their low weight, highly customizable properties, low cost, and energy efficiency [1]. At the same time, it is also understood that these materials can present a greater fire safety hazard than traditional building materials [2]. Thus, understanding their resistance and reaction to fire is crucial. A variety of standard test methods have been developed by organizations such as ASTM International [3,4] and UL [5,6] to assess material flammability in terms of ignitability, heat release and surface flame spread. Although these bench scale tests are widely used, they typically provide observations of material response to a specific set of conditions. Consequently, conflicting assessments often arise from different tests [7] and they show limited ability to predict material performance in other fire scenarios [8]. A more rigorous approach to assessing material flammability, which would allow for the proactive design of new, safer materials, is to characterize the controlling mechanisms of a fire behavior of interest and develop models that accurately describe these constituent processes. In this manner, the behavior of a material in response to a wide range of likely fire conditions can be better understood and predicted.

Upward, concurrent-flow flame spread over the surface of a material has long been recognized in the fire safety field as a highly important process because it is a key determinant of the initial rate of fire growth [9]. It has been well established [10,11] that surface flame spread is governed by positive feedback between transient processes of solid phase degradation (pyrolysis) and gas phase combustion. As a solid is heated, it degrades and produces gaseous pyrolyzates that can react with the ambient oxidizer to form a diffusion flame. Some of the heat produced by this flame is transferred back into the solid thus allowing for continued degradation and production of flammable pyrolyzates. Upward spreading flames may grow rapidly because hot combustion products, driven upward by buoyancy, heat up a part of the solid that is not yet degrading, which causes continuous expansion of the pyrolysis region.

* Corresponding author.
E-mail address: stolia@umd.edu (S.I. Stoliarov).

http://dx.doi.org/10.1016/j.combustflame.2017.02.007
0010-2180/

Early flame spread models (e.g. Grant and Drysdale [7] or Saito et al. [12]) attempted to provide an analytical solution for flame spread rate by relying on a number of coarse assumptions including constant flame height, a single value of flame to surface heat flux (to describe the entire flame heat feedback profile), and simplified treatments of decomposition and heat transfer in the solid phase. Despite these simplifications, these early models formed a solid foundation for later works that have incorporated more detailed descriptions of the constituent processes [13]. Development of generalized numerical pyrolysis models [14–16], which include submodels for chemical reactions, phase transitions, and transient heat transfer through the condensed phase characterized by temperature- and composition-resolved thermophysical properties, has opened new opportunities for further flame spread model development.

These opportunities were explored in our recent study [17] where a generalized numerical pyrolysis model, ThermaKin2D, was coupled with an empirical model of a flame spreading upward on 17.5 cm tall samples of poly(methyl methacrylate) (PMMA). The flame model was based on highly spatially resolved measurements of flame heat flux to the sample's surface and was formulated to compute the flame's heat feedback profile solely as a function of the width-normalized mass loss rate, which was calculated by the pyrolysis model. This unified model was shown to accurately predict flame spread dynamics and mass loss evolution of 4.0 and 17.5 cm tall PMMA samples, while using a small fraction of computational resources required for a computational-fluid-dynamics-based simulation of the same system [18].

A key limitation of this flame model was that it could only be applied to PMMA. In the current study, that limitation is removed. Spatially resolved measurements of flame heat flux and mass loss rate were obtained during upward flame spread over the surface of vertically oriented solid samples, which were up to 20 cm in height. Seven polymeric solids representing a wide range of chemical compositions and burning behaviors, including melt flow, sample burnout and heavy soot and solid residue formation, were utilized in these experiments. Heats of combustion of gaseous pyrolyzates produced by these materials were also measured. Several model parameter scaling approaches based on the established theory of flame structure were examined. The approach that provides the best agreement between experimental measurements and model predictions was identified.

2. Flame model formulation and scaling

Knowledge of heat transfer across the length of a flame into a burning material's surface is required to predict the rates of upward flame spread over that material [19]. Thus, in fire science, flame height is considered to be a critical parameter describing flame structure. Flame height has been defined in the literature in multiple ways: e.g. based on visual determination of the flame tip [12] or the average location of the visible flame [20], as the position corresponding to a critical fuel concentration [21], or based on a threshold value of wall heat flux [17]. Previous analysis of PMMA wall flames [22] revealed that wall heat flux at the flame tip is about 20% of the value in the continuous region. Thus, the location of luminous flame tips is not the ideal characteristic length scale for flame heat transfer. Consequently, in our previously developed PMMA flame model [17], we defined a "heat flux flame height", y_f, as the distance from the base of the flame to the highest point where measured wall flame heat flux is within 97.5% of its steady state value, q''_{steady}. q''_{steady} can be measured under the continuous region of the flame and it is, on average, within 2 kW m^{-2} of the maximum heat flux observed at that same location. Previously, y_f was related to width-normalized mass loss rate, $\frac{dm'}{dt}$; however, a multitude of experimental and theoretical observations [12,20,21,23,24] indicate that, for both laminar and turbulent buoyancy driven diffusion flames, including wall fires, flame height is a function of heat release rate. Therefore, it is expected that the relationship for this heat flux flame height scales with the ratio of the heats of combustion:

$$y_f = a\left(\frac{\Delta H_c^{MATL}}{\Delta H_c^{PMMA_{EXT}}}\frac{dm'}{dt}\right)^p + b \tag{1}$$

Here, ΔH_c^{MATL} represents the heat of combustion of the gaseous pyrolyzates of the material which is being modeled; $\Delta H_c^{PMMA_{EXT}}$ represents the heat of combustion of the pyrolyzates of extruded PMMA, the material for which this flame model was originally developed; and a, p, and b are empirically derived constants. In this expression, mass loss rate is divided by $\Delta H_c^{PMMA_{EXT}}$ because the constant a already implicitly includes this value and it is multiplied by ΔH_c^{MATL} to be converted to heat release.

Net flame heat flux, q''_{flame}, is expressed in our flame model in terms of y_f and several additional parameters:

$$q''_{flame} = \begin{cases} h_{flame}(T_{fl,\max}^{MATL} - T_{surf}) & \forall y \le y_f \\ h_{flame}\left(\alpha_f\left(T_{fl,\max}^{MATL} - T_{HFg}\right)e^{-\ln(\alpha_f)\times(y^*)^2} + T_{HFg} - T_{surf}\right) & \forall y > y_f \end{cases} \tag{2}$$

$$y^* = \frac{y + y_0}{y_f + y_0} \tag{3}$$

$$T_{fl,\max}^{MATL} = \begin{cases} T_{fl,\,adiabatic}^{MATL} & \forall \quad y \le 5\text{cm} \\ 0.87 \times T_{fl,\,adiabatic}^{MATL} & \forall \quad y > 5\text{cm} \end{cases} \tag{4}$$

For laminar wall flames, q''_{flame} has been shown to be primarily convective in nature [19]. Specifically, our previous measurements have shown that the radiative component of these flames accounts for less than 20% of total measured flame heat flux for $y_f \le 15$ cm [18]. Thus, in this model, q''_{flame} is defined based on a classical convection heat transfer expression. The impact of a "blowing effect" [25,26] (in which an increased flux of gaseous pyrolyzates increases flame standoff distance and reduces convective heat feedback) on measured heat transfer in this system was found to be minor [17,18,27] and thus it is not explicitly included in the model expressions.

In Eq. (2), h_{flame} is a heat transfer coefficient that captures both the dominant convective and minor radiative components of flame to surface heat transfer. h_{flame} is defined as a single constant value across the sample's surface; its calculation is detailed in a later section of this manuscript. $T_{fl,\,adiabatic}^{MATL}$ is the adiabatic flame temperature (in K) for the stoichiometric mixture of gaseous pyrolyzates and air, which has been shown to reasonably approximate the maximum temperature of laminar wall flames [17,28]. In the previously developed flame model, this temperature was computed for pyrolyzates of PMMA [17]. In this study, $T_{fl,\,adiabatic}^{MATL}$ was computed for each material of interest based on their respective ΔH_c^{MATL} values, which were measured using several techniques discussed in the following sections, together with the known atomic composition of their pyrolyzates.

$T_{HFg} = 291$ K is the average temperature of the water used to cool the heat flux gauge utilized for flame heat flux measurements and T_{surf} is the temperature (in K) of the surface into which the flame heat flux is calculated. When T_{surf} is set equal to T_{HFg}, Eq. (2) calculates flame heat flux as measured by the water-cooled heat flux gauge, q''_{HFg}. y is the distance downstream from the base of

Table 1
Materials used to obtain data for flame model generalization.

Material	Resin composition	Sample thickness (mm)	Manufacturer	Distributor
Acrylonitrile Butadiene Styrene (ABS)	$C_8H_8 \cdot C_4H_6 \cdot C_3H_3N$	6.2	Westlake Plastics	Modern Plastics
High Impact Polystyrene (HIPS)	C_8H_8	5.9	Spartech Plastics	Professional Plastics
Glass Filled Polybutylene Terepthalate (PBT)[a]	$C_{12}H_{12}O_4$	5.8	BASF	BASF
Cast Poly(Methyl Methacrylate) ($PMMA_{CAST}$)	$C_5H_8O_2$	6.1	Evonik Industries	Evonik Industries
Extruded Poly(Methyl Methacrylate) ($PMMA_{EXT}$)	$C_5H_8O_2$	5.8	Evonik Industries	US Plastic Corporation
Polyoxymethylene (POM)	CH_2O	6.7	Ensinger	Curbell Plastics
Polypropylene (PP)	C_3H_6	6.4	Compression Polymers Corporation	US Plastic Corporation
Glass Reinforced Unsaturated Polyester (UP)[a]	$C_8H_6O_2 \cdot C_8H_{16}O_4 \cdot C_5H_{12}O_2 \cdot C_4H_2O_3$	5.5	Prepared In-House from Fibre Glast Resin	–

[a] PBT and UP samples are glass-reinforced (25 and 50 wt%, respectively) composite materials.

the flame; α_f and y_0 are empirical constants. α_f defines the decay (curvature) of the flame heat feedback profile with respect to distance downstream of y_f. y_0 determines how far this heat feedback profile extends beyond y_f. Effectively, these parameters scale the gas temperature in the convective heat flux expression, which reflects the fact that the changes in the flame heat flux with the distance from the base of the flame are dominated by cooling of the buoyant plume through entrainment of surrounding air.

In addition to scaling flame height and peak flame temperature (y_f and $T^{MATL}_{fl,\,adiabatic}$, respectively) by ΔH_c^{MATL}, extension of the flame model to other materials required a redefinition of y (the distance downstream from the base of the flame). In the previously developed model, the location of the base of the flame was approximated as the position of the bottom of the solid sample even though, as samples continued burning, the base of the flame moved downward due to polymer melt flow. The error associated with this approximation was compensated for by adjusting parameters of Eq. (1); however, this approach made it impossible to directly extrapolate the flame model to materials for which flame base movement dynamics differs from that of extruded PMMA. Therefore, in the current study, $y = 0$ was redefined to correspond to the actual base of the flame. Measurements from experiments on extruded PMMA, which were the basis of the previously developed flame model, were thus re-analyzed by explicitly tracking the location of the base of the flame, y_b, with respect to the bottom of the sample throughout the duration of experiments. This new, more accurate definition of y resulted in changes in the flame model parameters a, p, b, α_f, and y_0 with respect to those reported in a previous publication [17].

3. Experimental

3.1. Materials

Most thermoplastic materials used in this study were purchased in the form of 6.0 ± 0.7 mm thick sheets, which were free of dyes or flame retardants. A summary of manufacturer and distributer information for each material is provided in Table 1. Two types of PMMA, extruded ($PMMA_{EXT}$) and cast ($PMMA_{CAST}$), were used to examine the potential impact of dripping and melt flow on flame spread measurements. Unlike $PMMA_{EXT}$, which was used to develop the original flame model, $PMMA_{CAST}$ did not exhibit melt flow or dripping due to its significantly higher average degree of polymerization. Samples of polybutylene terephthalate (PBT) and unsaturated polyester (UP) studied in this work contained inorganic reinforcement. PBT samples were prepared by BASF and contained 25 wt% of chopped glass fiber. UP samples were prepared in-house and contained 50 wt% of a plain weave glass fabric. A detailed description of the composite's manufacturing process is provided elsewhere [29].

The atomic composition of each polymer studied in this work is listed in Table 1. For all polymers, with the exception of UP resin, this information was obtained from the manufacturer. The UP resin is known to be synthesized from phthalic anhydride, maleic anhydride, and styrene, which polymerize into a thermosetting network of polyester chains with polystyrene crosslinks. However, the exact composition of the Fibre Glast UP resin is proprietary. Therefore, it was approximated by a known composition of a general purpose polymerized UP resin [30].

3.2. Upward flame spread experiments

To characterize the wall flames supported by materials listed in Table 1, experimental measurements of flame heat flux and sample mass loss rate were taken as a flame spread upward across the surface of 5–20 cm tall and 5 cm wide samples. Heat flux and mass loss rate measurements were obtained in separate tests to avoid potential interference between the corresponding diagnostic tools. Every test was videotaped.

All samples were mounted onto a 6.0 mm thick sheet of Kaowool PM insulation, and surrounded by a 2.5 cm wide strip of the same insulation at their top, bottom, and two sides. Samples and surrounding insulation pieces were fixed to the back insulation board using a thin (≈0.5 mm) layer of a high temperature 3 M Loctite epoxy. Prior to each test, sample-insulation assemblies were conditioned in a desiccator in the presence of Drierite for a minimum of 24 h.

At the beginning of each test, sample-insulation assemblies were secured within a holder that consists of two steel panels connected along one side by a hinge. When the front panel is closed around a sample, it is locked in place by four (top, bottom, and sides) clasps. Prepared samples are then secured in place by thumbscrews that press the insulation surrounding the sample into the backside of the front panel, thus exposing only the front surface of the sample slab as well as 2.0 and 0.5 cm, respectively, of insulation above/below and to either side. This holder design and sample mounting procedure is presented in detail elsewhere [18]. As shown in Fig. 1, the sample holder was placed beneath an exhaust hood to ensure the adequate removal of combustion products while maintaining nearly quiescent conditions (induced vertical air velocity of $\approx 0.05\ \mathrm{m\,s^{-1}}$). All samples were ignited at their base by a 5 cm wide, non-premixed gas burner, which was supplied with $0.15\ \mathrm{L\,min^{-1}}$ (at 1 atm and 298 K) of propane.

Burner flame heat flux, from the burner flame to a water-cooled Schmidt-Boelter heat flux gauge embedded flush with the sample's surface, was carefully measured in a previous study [17]. This heat

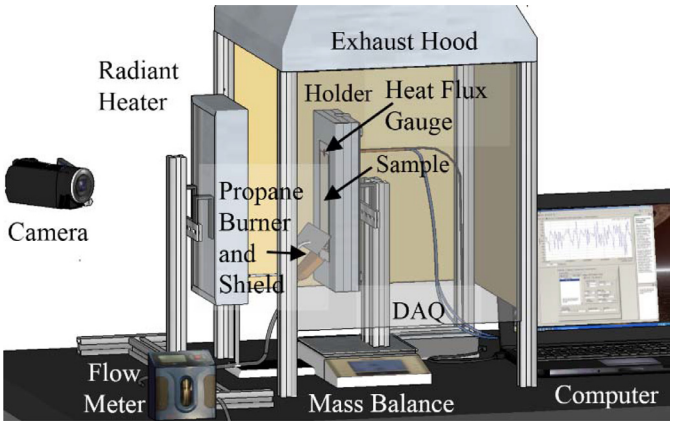

Fig. 1. Experimental setup for vertical burning and upward flame spread experiments.

flux was found to decrease with height above the bottom of the sample, y_s, from 50 kW m^{-2} at $y_s = 0$ to 27 kW m^{-2} at $y_s = 2$ cm. A steel shield positioned horizontally above the bottom of the sample (see Fig. 1) was used to limit the sample area exposed to the burner flame; above the shield, at $y_s > 2.5$ cm, measured burner flame heat flux was close to 0. Burner flame heat flux was fairly uniform across the width of the sample (less than 10% deviation from the center reading).

Tests began with ignition of the burner, which was kept in place just long enough for sustained, uniform ignition of each sample along its bottom edge. Immediately after sample ignition, the burner was removed and a radiant heater was positioned, if needed, to provide up to a 20 kW m^{-2} heat flux to the sample's front surface (as measured by a water-cooled heat flux gauge). This external heat flux, q''_{ext}, remained constant throughout the duration of tests and varied by less than 10% across the sample's front surface. Application of q''_{ext} was used to induce flame spread for materials that did not independently sustain the process. Samples were allowed to burn until completely involved, until steady state measurements of flame heat flux were recorded for at least 60 s, or until secondary burning behavior (e.g. polymer melt flow, sample burnout, or residue formation at the sample's surface) significantly impacted measurements. Samples were extinguished by application of a compressed air stream.

To measure sample mass loss rate, the sample holder was placed on top of a Mettler Toledo XS4002S balance, which recorded sample mass at a frequency of 1 Hz. Width-normalized mass loss rate, $\frac{dm'}{dt}$, was calculated as the numerical derivative of measured sample mass, using a 1 s time step, divided by flame width. For all materials with the exception of UP, the flame width was equal to the width of the sample (5 cm). In the case of UP, flame width reduced with time due to burnout along each side of the sample. Therefore, a video review was used to determine the evolution of flame width throughout the duration of experiments. Signal noise in $\frac{dm'}{dt}$ was reduced by applying a 5 s running average. For each material and sample height of interest, tests were repeated 3–6 times. Measurements from repeated tests were averaged together and this combined dataset was further smoothed using a 5 s running average prior to further analysis.

For flame heat flux measurements, samples were further prepared by drilling an orifice at the top and along the centerline (width) of the sample slab to allow a heat flux gauge to be tightly secured such that its face was flush with that of the slab and the surrounding insulation (above). A 0.95 cm diameter, Schmidt-Boelter heat flux gauge (manufactured by Medtherm) cooled with water at an average temperature of $T_{HFg} = 291$ K was employed in these measurements. The heat flux gauge was calibrated before each test and cleaned and repainted after every 1–3 tests, in accordance with the procedures described elsewhere [17]. Total flame heat flux measured by this water-cooled heat flux gauge, q''_{HFg}, was recorded at 2 Hz using an NI USB-9211A data acquisition module (DAQ) connected to a computer. For each material and sample height of interest, flame heat flux experiments were repeated 3 times. Measurements from repeated tests were averaged together and this combined dataset was smoothed using a 5 s running average.

To obtain spatially resolved measurements of flame heat flux, samples of different heights were prepared and ignited identically and q''_{HFg} was measured at the top of each one by a single gauge, while a flame spread across the sample's surface. Heat flux measurements recorded at the top of each smaller sample were used to represent those that would be obtained at the same location, y_s, on taller samples of the same material. Heat flux measurements taken at each location were related to $\frac{dm'}{dt}$ measurements from the tallest samples. A detailed justification of this equivalency is provided in earlier publications [17,27]. While this approach required a greater number of experiments, it prevented potential distortions in flame temperature and flow field associated with the simultaneous use of multiple water-cooled gauges and it eliminated the possibility of gauge damage due to polymer dripping or melt flow.

ABS and HIPS presented a unique challenge for flame heat flux measurements: the flames supported by these materials deposited large amounts of soot onto the sample and the surface of the heat flux gauge. This behavior is detailed in later sections of the manuscript. An attempt to mitigate soot deposition on the heat flux gauge by raising its water temperature to 348 K was unsuccessful. To assess the impact of this deposition on measured flame heat flux, additional measurements were performed where the heat flux gauge was shielded using a thin, custom cut and fitted piece of thermal insulation. This insulation shield prevented soot buildup on the surface of the gauge without affecting material burning dynamics. This shield was removed at different times after sample ignition and a 'clean gauge' measurement of flame heat flux was recorded as the maximum value measured within 5 s after shield removal.

Burning of HIPS, PMMA$_{EXT}$, POM, and PP samples was accompanied by a downward movement of the base of the flame due to melt flow. Conversely, burning of PBT and UP samples was accompanied by upward movement of the base of the flame due to burnout of the material near the bottom of the sample. These behaviors were quantified through video analysis. The location of the base of the flame (y_b) with respect to the bottom of the sample was tracked in time; it was taken to correspond to the lowest position of the continuous flame sheet that was at least as wide as 60% of the maximum flame width.

3.3. Heat of combustion measurements

The heats of combustion of the gaseous pyrolyzates produced by ABS, HIPS, PBT, PMMA$_{CAST}$, PMMA$_{EXT}$, POM, PP, and UP were measured using a Govmark CC-1 cone calorimeter built and calibrated (daily) in accordance with the ASTM 1354 standard [3]. Preliminary tests were performed to examine whether the heats of combustion were sensitive to sample orientation (horizontal versus vertical) and external radiant heat flux (q''_{ext}). In the vertical orientation, heat of combustion measurements were sensitive to the application of external heating. Therefore, comprehensive heat of combustion measurements were carried out in this orientation both in the presence and in the absence of external heating. In the horizontal orientation, heat of combustion measurements were not sensitive to the presence or absence of external heating. Thus, in this orientation, only measurements from tests conducted with external heating (as prescribed in the standard [3]) are reported. These experimental configurations and the magnitude of the ap-

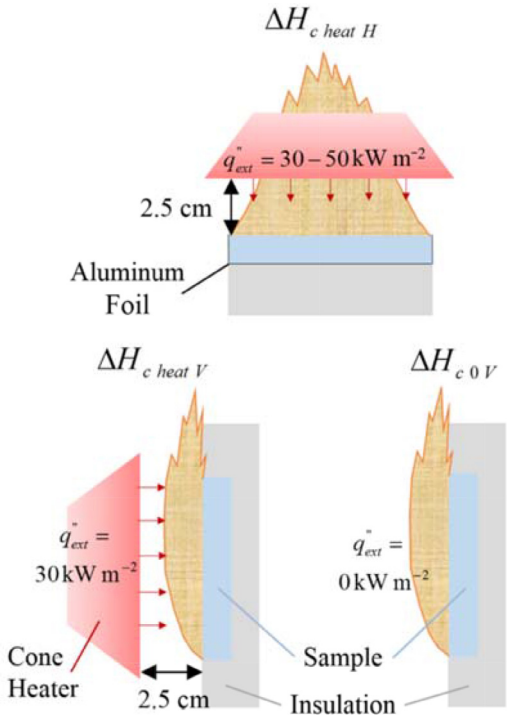

Fig. 2. Test configurations for heat of combustion measurements performed in a cone calorimeter.

plied external heat flux are shown in Fig. 2 together with the nomenclature for the corresponding heat of combustion values.

The majority of cone calorimeter tests were performed using 10 cm tall and 5 cm wide polymer samples; these dimensions match the average sample size used in flame spread experiments. Samples were mounted on Kaowool PM insulation in a manner similar to that employed in the flame spread experiments (see Section 3.2). Several tests were performed using square, 10 × 10 cm samples as recommended in the standard [3]. These tests did not produce statistically different results and were added to the overall data set.

In all experiments conducted using an external heat flux, samples were ignited by a standard cone calorimeter spark igniter positioned 13 mm away from (normal to) the center of the sample's front surface. In experiments conducted without external heating, samples were ignited outside of the cone calorimeter hood using a hand-held butane torch applied across the top sample surface and then moved under the hood (and onto the cone calorimeter mass balance platform) after a flame was established. Each material was tested in all three experimental configurations shown in Fig. 2; tests were repeated 2–4 times to accumulate statistics.

Heat release rate and mass loss rate histories generated in these experiments were utilized to compute the heats of combustion of the pyrolyzates. First, instantaneous heat of combustion was computed by dividing instantaneous heat release rate by the corresponding mass loss rate. Subsequently, a quasi-steady portion of the instantaneous heat of combustion dependence on time (t) was identified and averaged to obtain the final heat of combustion value, as demonstrated in Fig. 3. Early and late portions of the instantaneous heat of combustion curve were ignored because their unsteady behavior was attributed to errors (in particular, small time shifts) in the heat release and/or mass loss rate signals.

The heats of combustion of the gaseous pyrolyzates produced by ABS, HIPS, PBT, $PMMA_{CAST}$, $PMMA_{EXT}$, PP, and UP were also measured in microscale combustion calorimetry (MCC) [31] experiments. MCC heat of combustion values were obtained from several literature sources [29,32,33]. Unlike in the cone calorimeter,

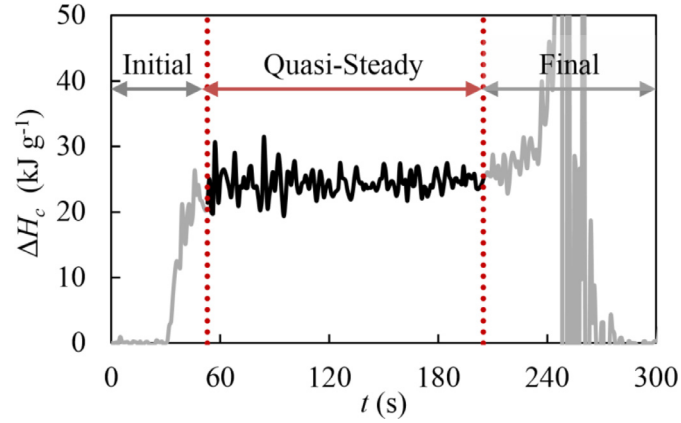

Fig. 3. Instantaneous heat of combustion calculated for a $PMMA_{CAST}$ sample burning in the horizontal configuration with q''_{ext} =50 kW m^{-2}.

where the pyrolyzates are combusted in a transitional diffusion flame, MCC utilizes a heated flow reactor where oxidation of the pyrolyzates is driven to completion in excess oxygen. This method provides heat of combustion values corresponding to a complete or near complete process, which are thus labeled in this manuscript as $\Delta H_{c\ complete}$. One exception is POM for which both MCC and cone calorimeter are known to yield somewhat inaccurate (low) values [34] because of a deviation from the empirical relation between oxygen consumption and heat release on which both methods are based. Therefore, for POM, $\Delta H_{c\ complete}$ was specified using the results of bomb calorimetry measurements [34].

4. Experimental results

4.1. Qualitative observations of material burning behavior

4.1.1. $PMMA_{CAST}$ and $PMMA_{EXT}$

Images of flame spread on $PMMA_{CAST}$ and $PMMA_{EXT}$ are shown in Figs. 4 and 5, respectively; timestamps in each figure (as well as those in Figs. 6–11) indicate time after sample ignition, $t - t_{ign}$. The burner application times for these and other materials are reported in a later section of the manuscript. To further clarify the coordinate system used in this work, distance above the bottom of the sample, y_s, the location of the base of the flame, y_b, and distance downstream from the base of the flame, y, are labeled in Figs. 4 and 5.

Within 10 s of ignition, PMMA flames grow to approximately 4–5 cm in height. A thin (<0.5 mm) layer of soot is observed to quickly form on the surface of the samples, downstream of the pyrolysis front, at $y_s > 4$ cm. This layer does not appear to impede flame spread but it effectively transforms PMMA slabs from clear to non-transparent. As the material continues burning, the flame grows and transitions away from purely laminar behavior (e.g. flickering is observed). For $PMMA_{CAST}$, the base of the flame remains fixed to the bottom edge of the sample throughout the duration of experiments. $PMMA_{EXT}$ samples exhibit mild melt flow. Approximately 180 s after ignition of this material, small, narrow polymer drips extend 1.5 cm below the bottom of the sample; 60 s later, drips begin intermittently falling from the sample to the base of the holder below. A quantitative analysis of movement of the base of the flame associated with this melt flow is provided in a later section of this manuscript.

4.1.2. PP and POM

PP and POM exhibited the most significant melt flow. PP samples were observed to flow downward at their bottom prior to ignition, during the burner application phase of the experiments.

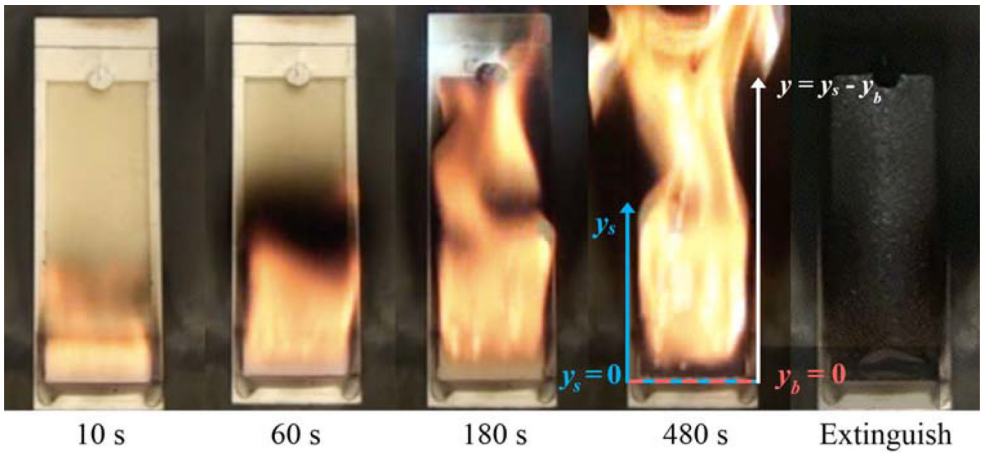

Fig. 4. Representative test of flame spread over a 15 cm tall sample of $PMMA_{CAST}$ (front view, $q''_{ext} = 0$).

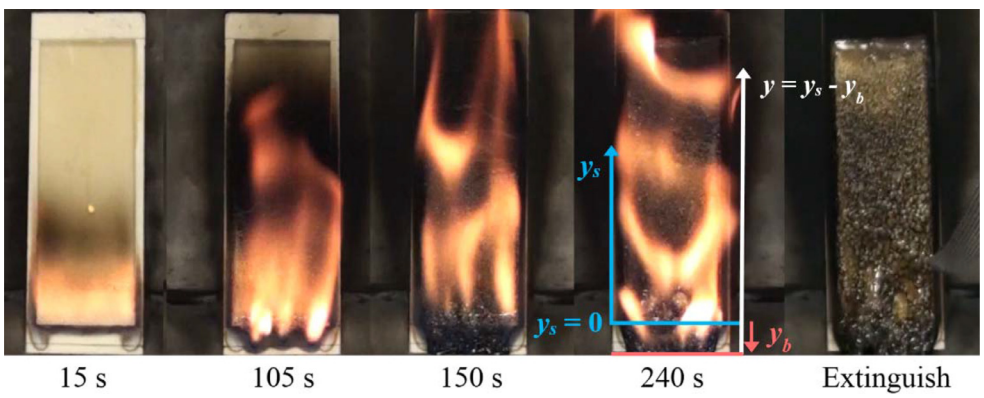

Fig. 5. Representative test of flame spread over a 20 cm tall sample of $PMMA_{EXT}$ (front view, $q''_{ext} = 0$).

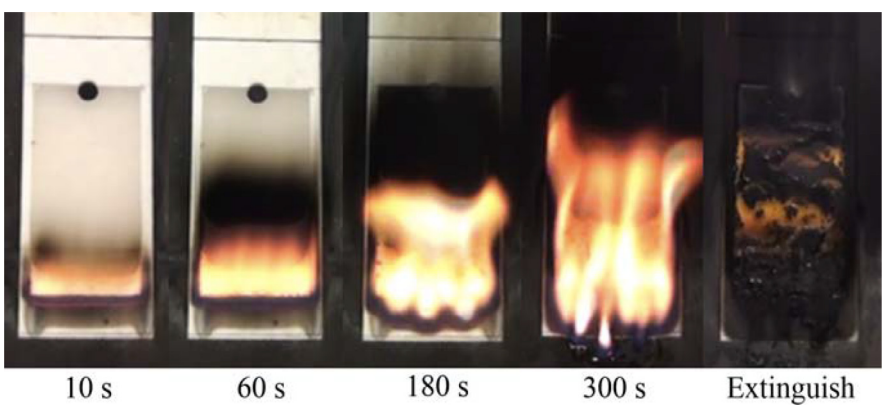

Fig. 6. Representative test of flame spread over a 10 cm tall PP sample (front view, $q''_{ext} = 0$).

For this material, at $t = t_{ign}$, the base of the flame was located 0.4 cm below the bottom edge of the sample slab, $y_b = -0.4$ cm. This behavior is consistent with this material's low melting point, 435 K [35]. Although PP samples melted readily, the base of the flame never extended beyond $y_b = -2$ cm. As seen in Fig. 6, as PP burned, a soot layer quickly formed at the material's surface, both directly beneath the flame and beyond the farthest reaches of flame tips. Although this soot layer remained relatively thin (<0.5 mm) throughout each test, it appeared to inhibit flame spread. During the early stages of tests, material degradation (e.g. sample softening or bubbling) was not observed beyond the region of the sample preheated by the propane burner. However, as PP samples continued burning, at approximately 450 s after sample ignition the front-most layer of the samples softened and slowly flowed downward thus fragmenting the attached soot layer. This fragmentation exposed the material behind the soot layer at which point the pyrolysis front was observed to advance. At later times in each test, melted PP began dripping from the sample slab to the base of the sample holder. The resulting drip pool did not burn and thus did not contribute to measured mass loss rate.

As seen in Fig. 7, POM samples maintained a transparent (soot-free) blue flame throughout the duration of tests. Shortly after ignition, POM supported a very small (approximately 1 cm tall) flame; however, within 180 s of ignition, a steady flame with tips extending up to $y_s = 6$–8 cm, was observed. At $t - t_{ign} \approx 280$ s, the pyrolysis front neared $y_s = 10$ cm. POM melt flow could be observed

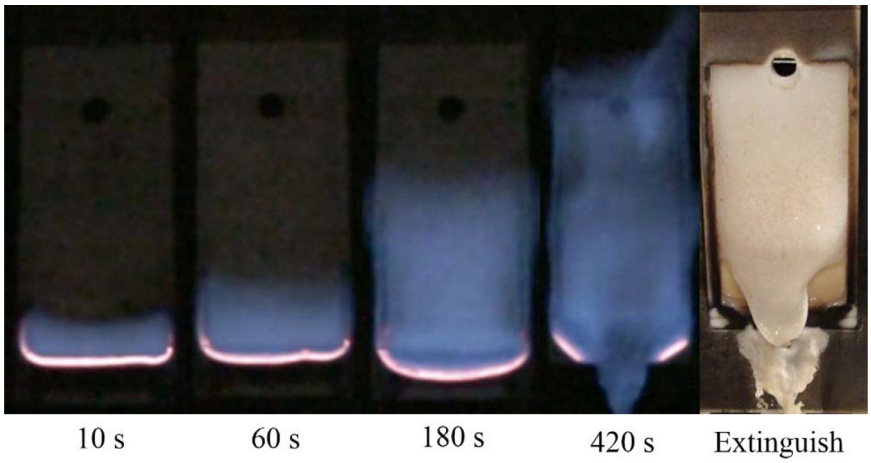

Fig. 7. Representative test of flame spread over a 10 cm tall POM sample (front view, $q''_{ext} = 0$).

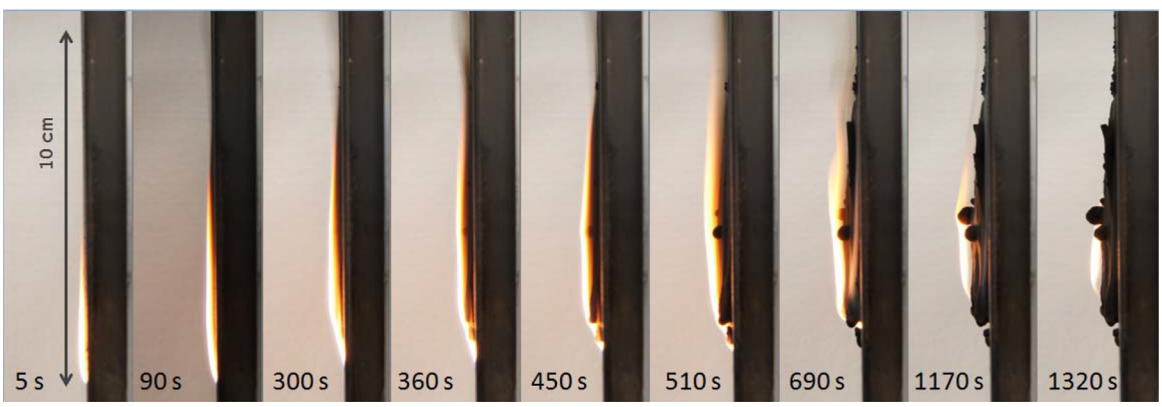

Fig. 8. Flame development on a 10 cm tall sample of ABS (side view, $q''_{ext} = 0$).

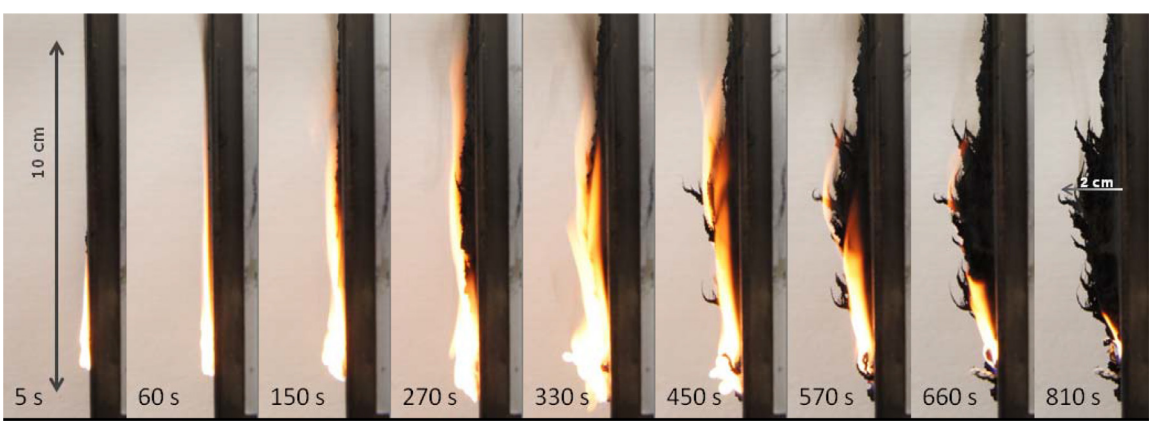

Fig. 9. Flame development on a 10 cm tall sample of HIPS (side view, $q''_{ext} = 0$).

shortly after ignition. This polymer melt continued to burn, allowing the base of the flame to progress downwards at a fairly steady rate until $t - t_{ign} \approx 365$ s. Between 390 and 430 s after ignition, a sudden and significant melt flow event was consistently observed – a lower portion of the sample (approximately 3 cm wide and 1.5 cm tall) quickly flowed down forming a flaming pool at the base of the sample holder. Shortly after this event, the experiment was stopped and the pool and wall flames were extinguished.

4.1.3. ABS and HIPS

ABS and HIPS produced the greatest amount of soot of all materials tests in this work. The soot produced by ABS flames readily adhered to the surface of the polymer to form a continuous dark layer across the full length of the sample within 10 s of ignition. As seen in Fig. 8, as ABS continued burning, soot continued to deposit creating a low density layer that measured at least 1 mm thick across the sample's surface within 120 s of ignition. Further soot deposition appeared to remain fairly uniform resulting in a 3–3.5 mm thick layer that was slightly thicker toward the bottom of the sample. Although a continuous 8–10 cm tall flame was observed for several minutes after sample ignition, in the absence of external heating, the soot layer inhibited progression of the pyrolysis front, ultimately causing sample extinction when the initial pyrolysis zone reached burnout. After extinction, a thin layer of char

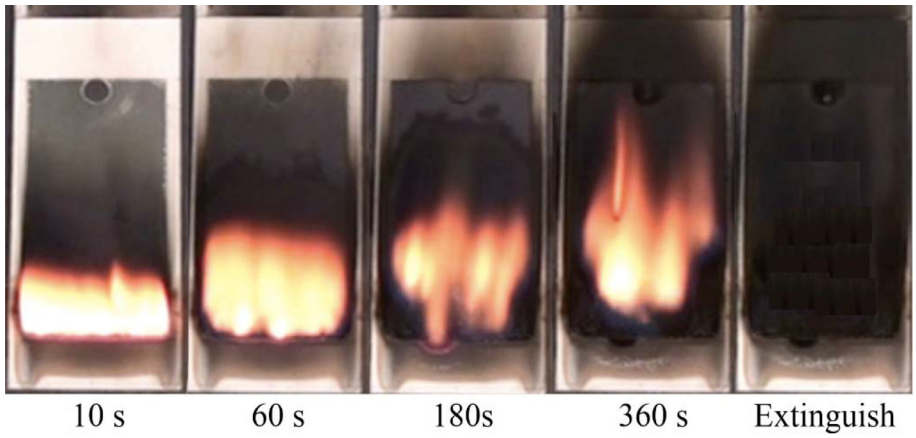

Fig. 10. Representative test of flame spread over a 10 cm tall UP sample (front view, $q''_{ext} = 0$).

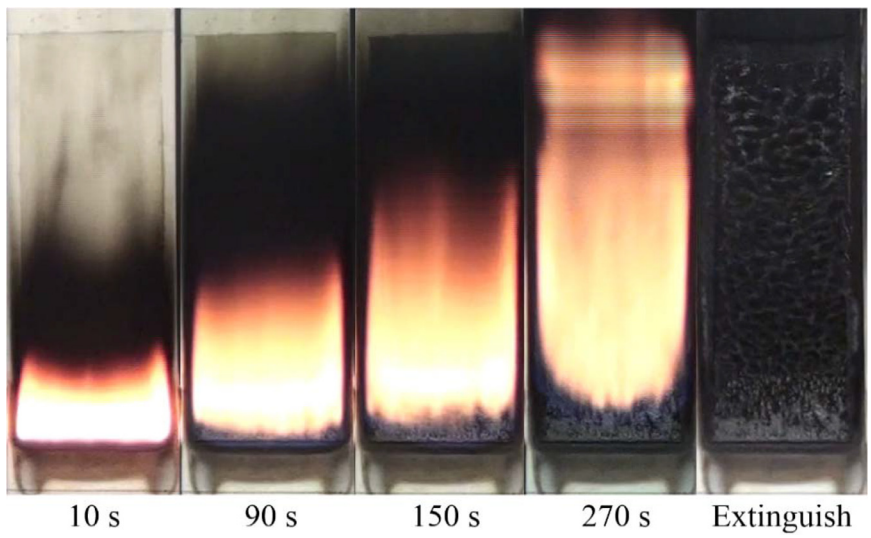

Fig. 11. Representative test of flame spread over a 14.5 cm tall PBT sample (front view, $q''_{ext} = 0$).

was observed at the material's front surface, behind the soot layer. Unlike the soot layer above, this char was rigid, porous, and firmly attached to the virgin ABS sample. The growth of the underlying char layer was difficult to track temporally; at extinction, this layer measured between 0.5 and 1 mm thick.

Applying a 10 kW m^{-2} radiant heat flux to ABS samples immediately after ignition induced flame spread over this material. Although heavy soot deposition was still observed in these tests, it did not prevent the pyrolysis front from advancing upward. Under these conditions, flame heat flux and sample mass loss rate were measured for up to 480 s after ignition.

In the case of HIPS, a soot layer also formed shortly after ignition. This layer extended beyond the flame tips but grew thickest directly beneath the flame. Unlike in the case of ABS, this soot layer did not grow uniformly to maintain a smooth surface. Instead, as seen in Fig. 9, thin strands of soot attached themselves to the sample (and the insulation and sample holder). Soot continued to agglomerate on these strands forming thicker and longer structures, which grew as far as 2 cm normal to the material's surface. During the early stages of soot layer growth on HIPS samples, flames could be found near the polymer's surface, in between individual soot strands. Although flames remained fairly uniform across the width of the sample as it burned, as this soot layer thickened, it produced an increasingly effective physical and thermal barrier that separated the flame from the polymer's surface, ultimately causing flame extinction. Numerous attempts were made to induce flame spread over HIPS samples (by applying up to 20 kW m^{-2} of external radiant heat flux and/or using a stronger ignition source). However, these attempts were unsuccessful. Therefore, HIPS data were collected in the experiments conducted without external heat flux during the first 180 s after sample ignition.

4.1.4. UP and PBT

Figure 10 shows images of flame spread over UP. At ignition, the flame was about 2 cm tall. Within 60 s of ignition, a thin layer of soot formed across the surface of the sample. As tests continued, the flame remained relatively weak and burnout was observed near the bottom and along the sides of samples resulting in a progressively narrower flame. Despite this burnout, samples maintained their original shape throughout experiments, leaving behind a residual structure (layers of glass fabric reinforcement). To avoid changes in burning behavior that could arise with very narrow flames, sample mass loss rate and flame heat flux measurements were analyzed only during the first 240 s after sample ignition, when the flame remained at least 4 cm wide.

Figure 11 shows flame spread over PBT. Within 90 s of ignition, flame tips were observed to reach $y_s = 6$ cm and a thin layer of soot had deposited farther downstream, across the full length

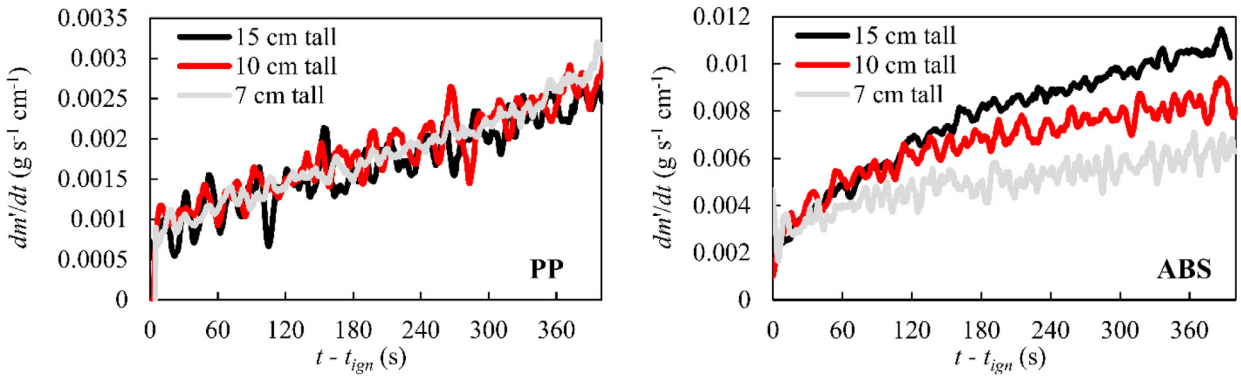

Fig. 12. Measured width-normalized mass loss rate of 7, 10, and 15 cm tall samples of PP ($q''_{ext} = 0$) and ABS ($q''_{ext} = 10\ \mathrm{kW\,m^{-2}}$).

of the sample. Although this soot layer developed quickly, it remained less than 1 mm thick and did not appear to inhibit flame spread. Throughout the duration of tests, the flame supported by PBT samples remained continuous and steady across its length. Burnout was first observed near the bottom corners of the sample, approximately 150 s after sample ignition. Due to the presence of chopped glass fibers, samples maintained their original shape throughout experiments and left behind a residual structure after burnout. Sample extinction occurred when burnout caused the base of the flame to advance toward the top of the sample. Shortly before sample extinction, PBT flames narrowed significantly. Therefore, the mass loss rate and flame heat flux data were collected only during the first 270 s after sample ignition, prior to the development of this behavior.

4.2. Mass loss rate

Measured width-normalized mass loss rates of 7, 10, and 15 cm tall samples of PP and ABS are plotted as a function of time after ignition in Fig. 12. For PP, $\frac{dm'}{dt}$ of samples of all three heights are essentially identical throughout the first 400 s after ignition, which indicates that the pyrolysis front does not advance beyond $y_s = 7$ cm. This behavior is consistent with qualitative observations discussed in Section 4.1.2. For ABS (studied at $q''_{ext} = 10\ \mathrm{kW\,m^{-2}}$), $\frac{dm'}{dt}$ of samples of all three heights are identical until approximately 45 s after ignition, at which point, measured mass loss rate of 7 cm tall samples no longer continues to increase at the same rate as that of larger samples. Later in the tests, approximately 120 s after ignition, the measured mass loss rate curve of 10 cm tall ABS samples similarly breaks away and no longer continues to increase at the same rate as that of 15 cm tall samples. These results further confirm an earlier observation [17,27] that the development of the pyrolysis zone during flame spread over a material is not altered between samples of different heights, provided that the samples are ignited and allowed to burn identically.

Figure 13 presents measured mass loss rate histories of the tallest samples of each of the materials studied in this work. For $\mathrm{PMMA_{EXT}}$, $\frac{dm'}{dt}$ from the second tallest, 17.5 cm tall, samples are used here as these samples showed greater resistance to melt flow. Solid lines are used in this figure to indicate experimental measurements (average of 3–6 repeated tests). Error bars plotted here were computed as two standard deviations of the mean. Dashed lines represent fitted curves, which smooth these measurements for further analysis. The fitted curves are piecewise defined by a series of second to fifth order polynomials of the form:

$$\frac{dm'}{dt} = c_0 + c_1(t - t_{ign}) + c_2(t - t_{ign})^2 + c_3(t - t_{ign})^3 + c_4(t - t_{ign})^4 + c_5(t - t_{ign})^5 \quad (5)$$

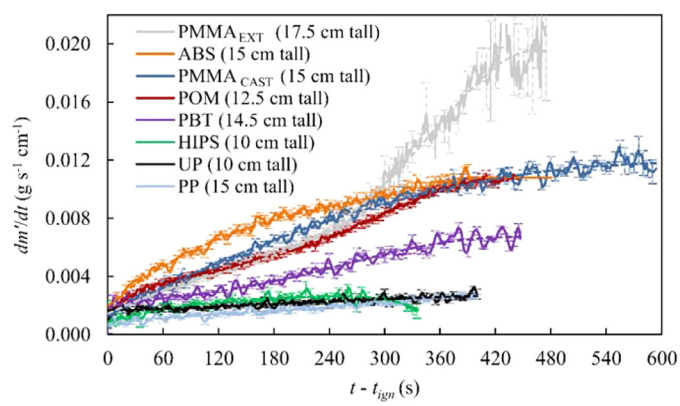

Fig. 13. Width-normalized sample mass loss rates of the tallest samples of each material studied in this work (with the exception of $\mathrm{PMMA_{EXT}}$). Solid lines are averaged experimental data; dashed lines are curve fits. All measurements were collected at $q''_{ext} = 0$, with the exception of the data for ABS, which was obtained at $q''_{ext} = 10\ \mathrm{kW\,m^{-2}}$. Here, error bars indicate two standard deviations of the mean.

The coefficients of the polynomials (c_0–c_5), the time ranges of their validity, and the ignition times (t_{ign}) of each material are provided in Table SI-1 of the Supplementary information document.

4.3. Flame heat flux

Figure 14 shows time-resolved heat flux – from flame to a water-cooled heat flux gauge, q''_{HFg} – measured (average of three tests) during upward flame spread over ABS, HIPS, PBT, $\mathrm{PMMA_{CAST}}$, $\mathrm{PMMA_{EXT}}$, POM, PP and UP. For most materials, q''_{HFg} was measured in several locations y_s (distance from the bottom of the sample), which are indicated on the figure. The displayed error bars were computed as two standard deviations of the mean (some error bars are comparable with the size of the symbols). As expected, q''_{HFg} tends to increase with time before reaching a steady value as the flame spreads toward the gauge. It takes progressively longer for peak, steady flame heat fluxes to be recorded at higher y_s, the delay corresponding to the additional time needed for the flame to reach that measurement location.

For ABS and HIPS samples, continuously measured q''_{HFg} values do not remain steady later in the experiments and instead show a significant decrease with time after a peak value is recorded. This decrease can be attributed to the soot layer that forms on the surface of each material as they burn and a similar layer that forms on the heat flux gauge's surface. The results of experiments designed to remove the effects of soot deposition on ABS and HIPS flame heat flux readings are shown in Fig. 14 as discrete data points labeled 'Clean Gauge'. These heat flux values are comparable to those

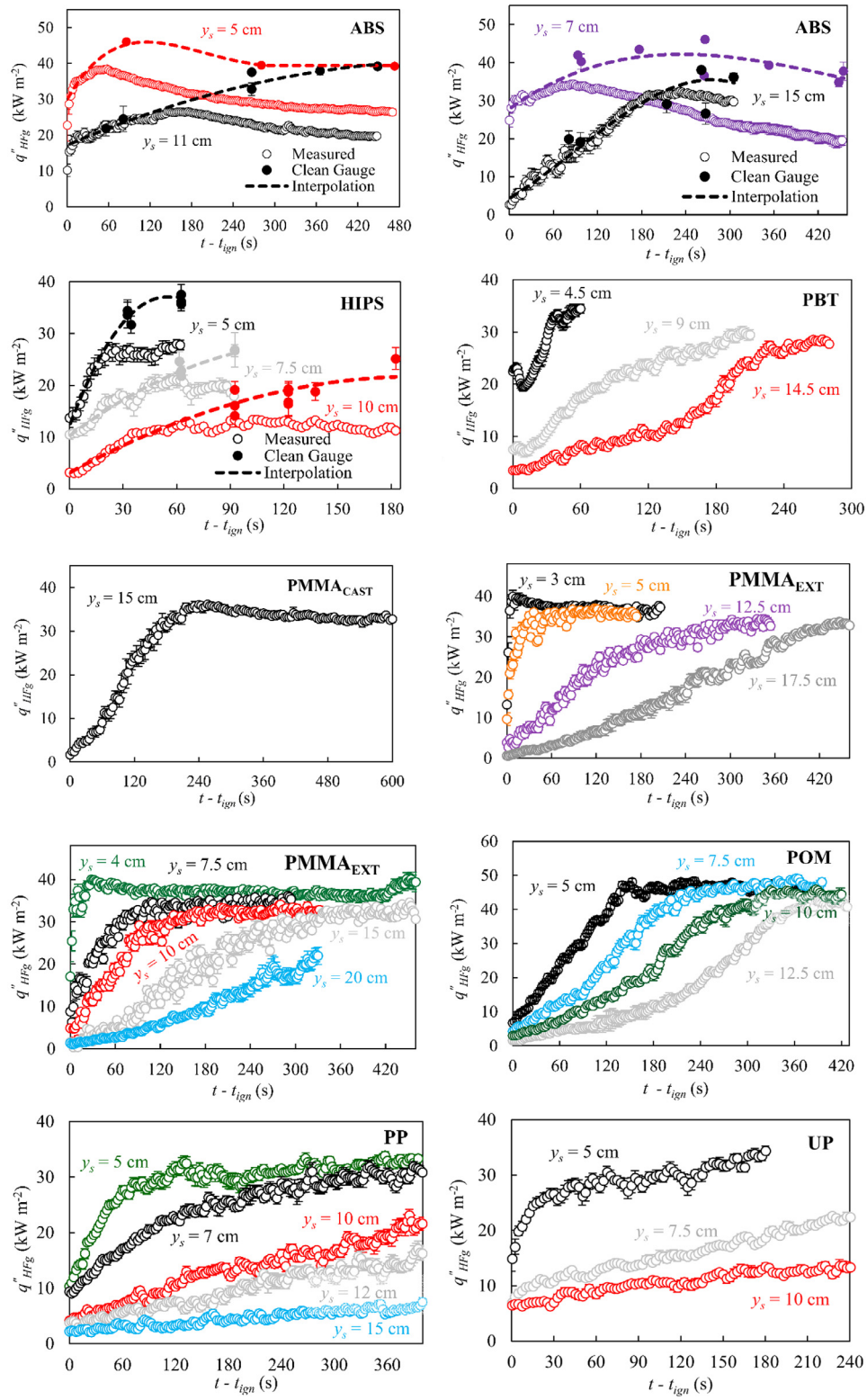

Fig. 14. Experimentally measured flame heat flux (to a water-cooled gauge) for ABS, HIPS, PBT, PMMA$_{CAST}$, PMMA$_{EXT}$, POM, PP, and UP materials at multiple locations, y_s, above the bottom of the sample. Here, error bars indicate two standard deviations of the mean.

continuously measured in the beginning of the experiments. However, the clean gauge readings become up to 20 kW m^{-2} higher at later times. These discrepancies indicate that the thermally insulating effect of the layer forming on the gauge is significant. To reconstruct ABS and HIPS flame heat flux histories that are nearly free from the effects of this soot layer, heat flux measurements obtained early in the experiments, while q''_{HFg} increases by at least 0.05 kW m^{-2} s^{-1}, were combined with the clean gauge data points and interpolated with spline functions, which are shown as dashed lines in Fig. 14.

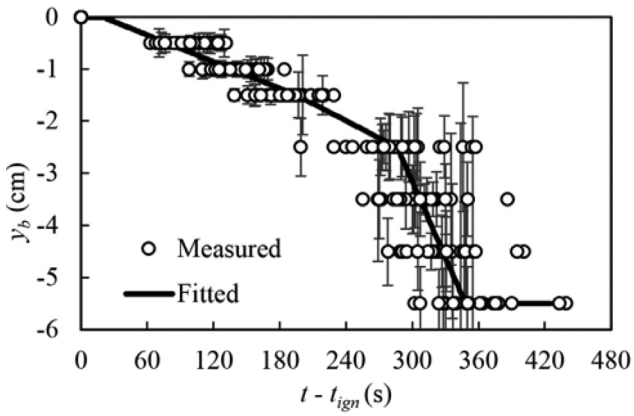

Fig. 15. Changes in the flame base location with time during upward flame spread over $PMMA_{EXT}$. Here, error bars indicate two standard deviations of the mean.

Table 2
Heats of combustion of gaseous pyrolyzates in kJ g^{-1}.

Material	$\Delta H_{c\ complete}$	$\Delta H_{c\ heat\ H}$	$\Delta H_{c\ heat\ V}$	$\Delta H_{c\ 0\ V}$
ABS	36.5 [32]	28.4 ± 0.7	29.3 ± 0.8	31.0 ± 0.9
HIPS	39.2 [32]	27.9 ± 0.7	30.2 ± 0.8	30.1 ± 0.3
PBT	23.1 [33]	21.6 ± 0.3	21.2 ± 1.1	20.2 ± 0.2
$PMMA_{CAST}$	24.5 [32]	24.4 ± 0.4	24.0 ± 0.4	21.3 ± 0.5
$PMMA_{EXT}$	24.5 [32]	23.8 ± 0.2	24.2 ± 0.1	20.0 ± 0.6
POM	15.9 [34]	14.9 ± 0.2	14.6 ± 0.6	11.8 ± 0.8
PP	41.0 [32]	37.9 ± 0.4	37.7 ± 0.4	31.7 ± 1.7
UP	22.7 [29]	20.5 ± 0.5	20.4 ± 1.0	23.4 ± 1.1

4.4. Flame base movement

For all materials studied in this work with the exception of ABS and $PMMA_{CAST}$, as samples burned, the base of the flame either moved upward, due to sample burnout, or downward, due to polymer melt flow. The location of the base of the flame, y_b, was thus tracked by video review throughout the duration of experiments. As was already mentioned, y_b is defined as the lowest position at which the flame is at least 60% of its maximum width. The evolution of y_b for $PMMA_{EXT}$ is shown in Fig. 15. Note that the base of the flame never extends below $y_b = -5.5$ cm as this location corresponds to the lower edge of the sample holder. Experimental measurements (open circles) obtained from all tests on 17.5 cm tall samples of $PMMA_{EXT}$ are plotted together and fitted piecewise with linear functions of the form:

$$y_b = d_0 + d_1\left(t - t_{ign}\right) \tag{6}$$

The function coefficients (d_0 and d_1) and the time ranges of their validity are reported in Table SI-2 of the Supplementary information document. This table also contains similar results for all materials tested in this work for which movement of the base of the flame was significant. Error bars in Fig. 15 were computed as two standard deviations of the mean when a minimum of three experimental measurements of y_b were recorded within a ±3 s period. For each material tested in this work, throughout the duration of experiments, fitted y_b expressions match experimental measurements, on average, within 0.5 cm.

4.5. Heat of combustion

The heats of combustion of gaseous pyrolyzates of the studied materials are summarized in Table 2. These data are also plotted in Fig. 16 to highlight the impact of burning conditions on heat release. The reported uncertainties were calculated as two standard deviations of the mean.

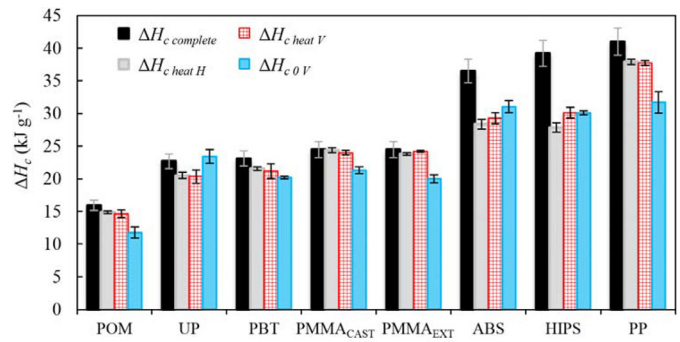

Fig. 16. Heats of combustion of gaseous pyrolyzates. Here, error bars indicate two standard deviations of the mean.

As expected, the MCC and bomb calorimetry measurements (reported as $\Delta H_{c\ complete}$) yield the highest heat of combustion values for all materials (except for UP, for which $\Delta H_{c\ complete}$ and $\Delta H_{c\ 0\ V}$ are equivalent within their respective uncertainties). Cone calorimeter measurements conducted in the presence of external heating produce similar values for horizontal and vertical sample orientations ($\Delta H_{c\ heat\ H}$ and $\Delta H_{c\ heat\ V}$). However, for POM, $PMMA_{CAST}$, $PMMA_{EXT}$, and PP, experiments conducted in the vertical orientation in the absence of external heating, which most closely mimic flame spread experiments, yield heats of combustion, $\Delta H_{c\ 0\ V}$, that are significantly (by about 15%) lower than the corresponding $\Delta H_{c\ heat\ H}$ and $\Delta H_{c\ heat\ V}$ values. These reductions in the heats of combustion correlate with increases in carbon monoxide yields as discussed in detail elsewhere [36].

These lower heats of combustion are speculated to be a result of partial thermal quenching of the flame near the material surfaces. Unlike in the case of cone calorimetry tests conducted with external heating, where the entire surface of the sample is ignited simultaneously, in vertical tests conducted without external heating, samples are ignited at their base and a flame gradually propagates upward. This flame comes in contact with a comparatively cooler solid surface that is below its pyrolysis temperature, which is thought to cause partial quenching of the flame. This effect is not observed for UP, PBT, ABS, and HIPS because an inorganic reinforcement and/or soot layer that quickly forms on the surface of these materials acts as a thermal insulator effectively shielding the flame from the bulk of the solid.

5. Flame model parametrization

5.1. Heat flux flame height

Previously measured $PMMA_{EXT}$ data [17] representing the dependence of heat flux flame height (y_f) on $\frac{dm'}{dt}$ are shown in Fig. 17 as red diamonds. These measurements were obtained under the assumption that the base of the flame remained fixed to the bottom of the sample. Adjusting these measurements for the downward movement of the base of the flame (which was quantified in Section 4.4) yields a new data set, which is shown on Fig. 17 as black squares. Error bars for each dataset indicate two standard deviations of the mean, as calculated based on a propagation of errors resulting from variation in time when y_f reaches a given location and uncertainties in y_b and $\frac{dm'}{dt}$. Fitting these data with Eq. (1) (solid line in Fig. 17) produces the following parameter values: $a = 190\ \text{cm}^{1.46}\ \text{s}^{0.46}\ \text{g}^{-0.46}$, $p = 0.46$, $b = -6.9$ cm. The values of these empirical constants defined here differ from those reported in our previous work [17]; however, as seen in Fig. 17, in either model, predicted dependence of y_f on sample mass loss rate is nearly identical for $y_f \leq 10$ cm. Primarily, the difference between

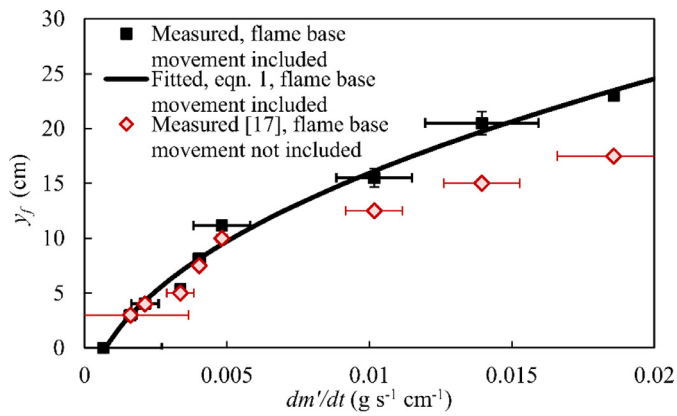

Fig. 17. Impact of flame base movement on heat flux flame height (y_f) dependence on mass loss rate. All data were obtained from flame spread experiments on $PMMA_{EXT}$. Here, error bars indicate two standard deviations of the mean. (For interpretation of the references to color in this figure, the reader is referred to the web version of this article.)

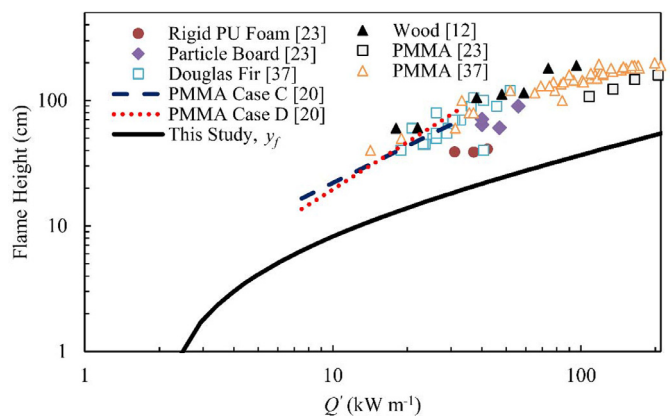

Fig. 18. Comparison of the heat flux flame height correlation developed in this work to literature data on flame height derived from visual observations and/or flame image analysis.

the two models arises at larger y_f (and at higher burning rates), which were observed later in experiments when downward movement of the base of the flame became significant.

The new correlation for y_f can be compared to literature data by plotting measured heat flux flame height values against width-normalized heat release rate, Q', which was computed as a product of the mass loss rate ($\frac{dm'}{dt}$) and $\Delta H_{c\ complete}$ of $PMMA_{EXT}$. This plot is shown in Fig. 18 along with a collection of literature data from several experimental studies of vertical wall flames fueled by combustible solids [12,20,23,37]. The current study is unique in that it offers data for very small flames ($y_f < 8$ cm). Qualitatively, the heat flux flame height correlation (Eq. (1)) developed in this work exhibits a trend similar to the literature data; however, the absolute values of y_f computed using this correlation are systematically lower than flame heights reported in the literature. This discrepancy is believed to be associated with differences in definition and measurement methodology. For the literature data presented here, flame height is defined based on visual observations and/or flame image analysis as the farthest extent of the continuous flaming region or visible flame tips; whereas in the current study, y_f is defined based on peak measured heat feedback in the continuous region of the flame (as explained in Section 2). This is further illustrated in Fig. 19, which demonstrates how using different criteria to define flame height can easily lead to a factor of two difference in reported values. In this figure, the heat flux flame

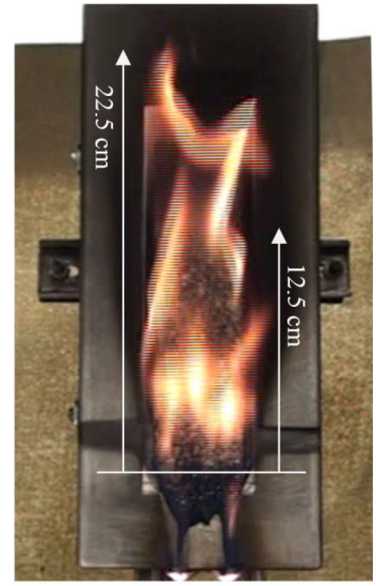

Fig. 19. Comparison of visually defined (left arrow) and heat flux based (right arrow) flame heights. Measurements indicate distance from the bottom of sample, y_s.

height reaches $y_s = 12.5$ cm; however, visible flame tips extend beyond $y_s = 22.5$ cm.

5.2. Flame heat flux shape

Using $T^{MATL}_{fl,\,adiabatic} = 2363$ K and $h_{flame} = 0.0193$ kW m^{-2} K^{-1} as previously computed for $PMMA_{EXT}$ [17] and the new flame height correlation, the flame heat flux histories obtained for this material were refitted to determine new values for the parameters α_f and y_0, which define the shape of the upper (decaying) portion of the flame heat flux profile as per Eqs. (2) and (3). This fitting process is described in detail in a previous publication [17]. The new values of α_f and y_0 were determined to be 1.79 and 3.75 cm, respectively. As show in Fig. 20, this newly parameterized flame model provides an excellent description of the $PMMA_{EXT}$ heat flux histories with no systematic over or under estimation of the time-resolved data. Note that, while the flame heat flux measurement locations shown on the figure (y_s) define distance with respect to the stationary sample bottom, the calculated heat flux profiles do take into account the movement of the base of the flame (i.e., y in Eqs. (2)–(4) is equal to $y_s - y_b$).

5.3. Extension to other materials

As argued in Section 2, extension of this flame model to an arbitrary material can be accomplished by using the heat of combustion of the gaseous pyrolyzates of the material of interest (ΔH_c^{MATL}) to scale the flame height correlation (Eq. (1)) and to compute the adiabatic flame temperature ($T^{MATL}_{fl,\,adiabatic}$) for the stoichiometric mixture of these gaseous pyrolyzates and air. $T^{MATL}_{fl,\,adiabatic}$ can be estimated using ΔH_c^{MATL} and the atomic composition of the pyrolyzates, which, in this work, was taken to be equal to that of the polymer (polymer compositions are listed in Table 1). To compute $T^{MATL}_{fl,\,adiabatic}$, the combustion products were assumed to consist only of CO_2, H_2O, and N_2 (no minor species); their temperature dependent heat capacities were obtained from the NIST Chemistry Webbook [38].

To determine which quantities best represent ΔH_c^{MATL}, five different methods were examined. In Methods 1, 2, and 3, ΔH_c^{MATL} was set to be equal to $\Delta H_{c\ complete}$, $\Delta H_{c\ heat\ H}$, and $\Delta H_{c\ 0\ V}$, re-

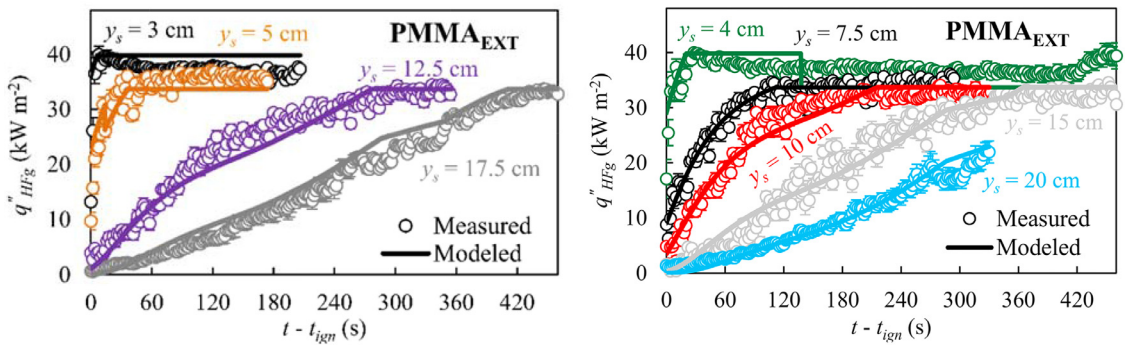

Fig. 20. Experimental and modeled flame heat flux histories for PMMA$_{EXT}$. Here, error bars indicate two standard deviations of the mean.

Table 3
Global radiative fractions, χ_r, measured using a fire propagation apparatus (FPA) and cone calorimeter.

Material	FPA	Cone calorimeter	Average
ABS	0.51 [41]	0.41 [42]	0.46
HIPS	0.50[a] [39,40]	0.49 [42]	0.50
PBT	0.30 [41]	–	0.30
PMMA$_{CAST}$	0.33 [39,40]	0.33 [42]	0.33
PMMA$_{EXT}$	0.33 [39,40]	0.33 [42]	0.33
POM	0.22 [39,40]	0.22 [42]	0.22
PP	0.39 [39,40]	0.57 [42]	0.48
UP	0.32 [39,41]	–	0.32

[a] HIPS χ_r values reported here are obtained from FPA measurements of polystyrene (PS).

Table 4
Flame model parameters computed using different heat of combustion definitions.

ΔH_c^{MATL}:	$\Delta H_{c\ complete}$	$\Delta H_{c\ heat\ H}$	$\Delta H_{c\ 0\ V}$	$(1-\chi_r) \times \Delta H_{c\ heat\ H}$
h_{flame} (kW m^{-2} K^{-1}):	0.0196	0.0201	0.0235	0.0288
Material			$T_{fl,\ adiabatic}^{MATL}$ (K)	
ABS	2410 ± 90	1980 ± 40	2120 ± 40	1260 ± 20
HIPS	2460 ± 100	1890 ± 30	2000 ± 10	1150 ± 20
PBT	2290 ± 90	2170 ± 20	2060 ± 20	1660 ± 10
PMMA$_{CAST}$	2330 ± 90	2320 ± 30	2090 ± 30	1710 ± 20
PMMA$_{EXT}$	2330 ± 90	2280 ± 20	1990 ± 40	1680 ± 10
POM	2410 ± 90	2290 ± 20	1910 ± 100	1890 ± 20
PP	2290 ± 90	2160 ± 20	1880 ± 80	1330 ± 10
UP	2320 ± 90	2140 ± 40	2370 ± 90	1600 ± 30

spectively. $\Delta H_{c\ complete}$ represents the upper bound of the heat of combustion. $\Delta H_{c\ heat\ H}$ values take into account combustion inefficiencies associated with transitional buoyant diffusion flames; $\Delta H_{c\ heat\ H}$ measurements are available for a wide range of materials. Finally, $\Delta H_{c\ 0\ V}$ values most closely correspond to the flame spread problem geometry and, as discussed in Section 4.5, take into account additional combustion inefficiencies associated with this particular experimental configuration.

In Method 4, an attempt was made to account for the flame's radiative losses by setting $\Delta H_c^{MATL} = (1-\chi_r) \times \Delta H_{c\ heat\ H}$, where χ_r is the global radiative fraction. In this work, χ_r was calculated as the average of measured values reported by Tewarson [39–41] and Quintiere et al. [42]; these values are listed for each material in Table 3. Here, χ_r is calculated as radiative heat release divided by chemical (total measured) heat release. It should be noted that, in the context of this method, the $T_{fl,\ adiabatic}^{MATL}$ parameter cannot be referred to as an adiabatic flame temperature. Nevertheless, for simplicity, the same parameter abbreviation was retained.

In Method 5, a hybrid approach was pursued where $(1-\chi_r) \times \Delta H_{c\ heat\ H}$ was used to scale the flame height correlation, while $\Delta H_{c\ complete}$ was employed to compute $T_{fl,\ adiabatic}^{MATL}$. The logic behind this method was that, while the overall flame is a subject of combustion inefficiencies and radiative losses, the hottest region of the flame (located near the flame base and represented by $T_{fl,\ adiabatic}^{MATL}$) may still correspond to nearly complete combustion accompanied by little soot production and, thus, insignificant radiative emissions. $T_{fl,\ adiabatic}^{MATL}$ values computed from the different heat of combustion definitions are summarized in Table 4. For consistency, $\Delta H_c^{PMMA_{EXT}}$ and $T_{fl,\ adiabatic}^{MATL}$ of PMMA$_{EXT}$ were also redefined in accordance with each method and the values of h_{flame} were recalculated (and reported in Table 4) to ensure that the model predictions of peak, steady heat flux of PMMA$_{EXT}$ flames (shown in Fig. 20) remain unaltered regardless of the method selection. Uncertainties provided in this table are calculated assuming that the primary source of error in calculated flame temperatures arises only from a propagation of error in measured ΔH_c^{MATL}.

The relative performance of these five methods was evaluated by computing the flame heat flux histories at different locations,

Table 5
Absolute differences in kW m^{-2} between predicted and measured flame heat fluxes. The differences calculated for each material were averaged throughout the duration of experiments and across all measurement locations.

	Method 1	Method 2	Method 3	Method 4	Method 5
y_f calculated from:	$\Delta H_{c\ complete}$	$\Delta H_{c\ heat\ H}$	$\Delta H_{c\ 0\ V}$	$(1-\chi_r) \times \Delta H_{c\ heat\ H}$	$(1-\chi_r) \times \Delta H_{c\ heat\ H}$
$T_{fl,\ adiabatic}^{MATL}$ calculated from:	$\Delta H_{c\ complete}$	$\Delta H_{c\ heat\ H}$	$\Delta H_{c\ 0\ V}$	$(1-\chi_r) \times \Delta H_{c\ heat\ H}$	$\Delta H_{c\ complete}$
Material	Absolute difference between predicted and measured flame heat fluxes (kW m^{-2})				
ABS	5.2	6.8	5.6	13.0	3.4
HIPS	3.8	9.1	2.4	16.1	12.4
PBT	5.2	5.0	6.3	3.3	5.2
PMMA$_{CAST}$	2.1	2.0	2.1	2.0	1.9
POM	7.4	7.8	8.7	7.0	7.8
PP	1.7	2.1	2.2	8.1	5.7
UP	1.7	4.0	11.1	6.1	3.3
Mean, all materials	**3.8**	**5.3**	**5.5**	**7.9**	**5.7**

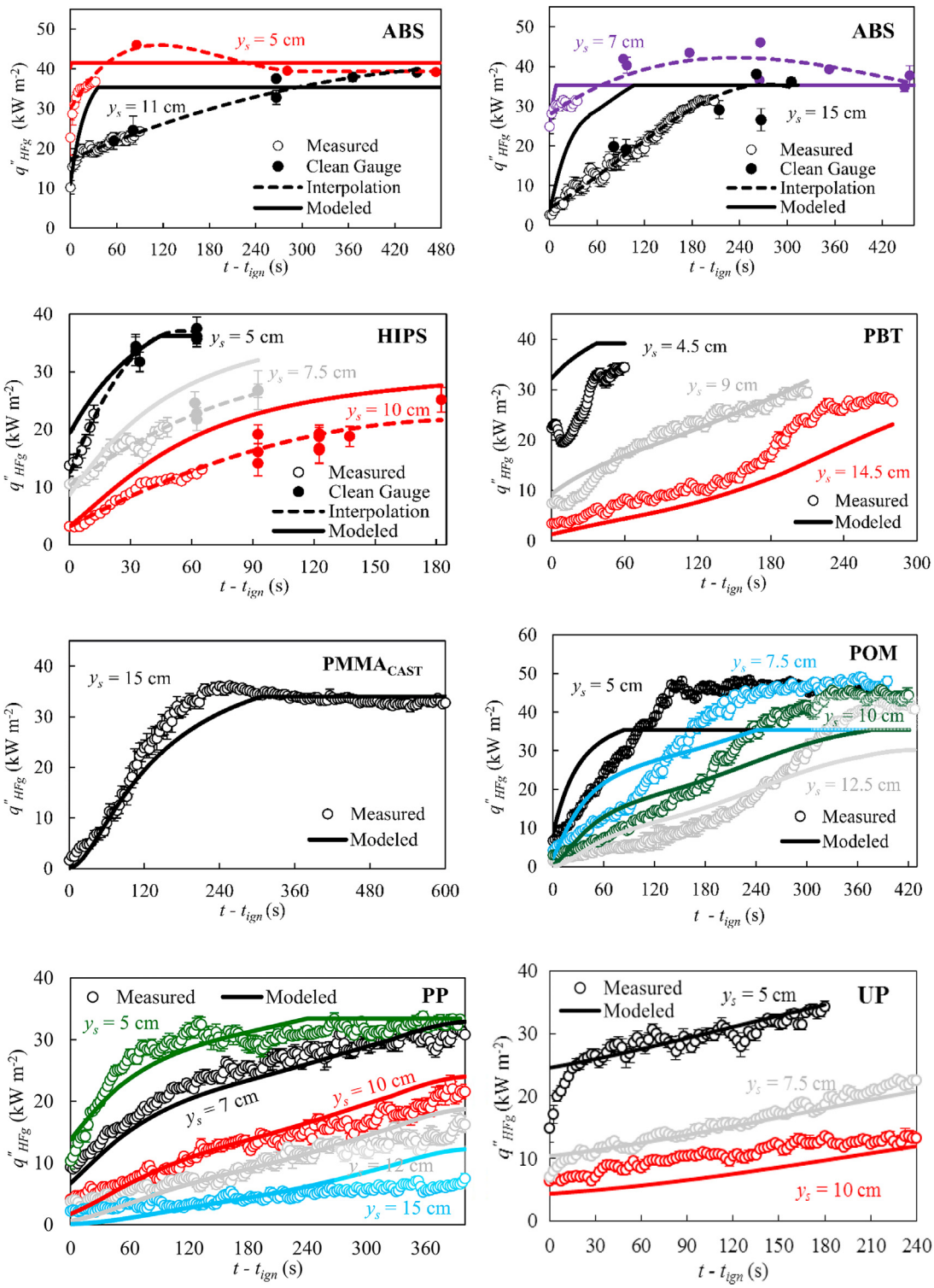

Fig. 21. Experimental and modeled flame heat flux histories for ABS, HIPS, PBT, PMMA$_{CAST}$, POM, PP, and UP. The model parameters were computed using Method 1. Here, error bars indicate two standard deviations of the mean.

y_s, for ABS, HIPS, PBT, PMMA$_{CAST}$, POM, PP, and UP (from the $\frac{dm'}{dt}$ and y_b curves defined by Eqs. (5) and (6)) and by comparing these heat fluxes to the corresponding experimental data. A summary of these comparisons is provided in Table 5. This table reports the average absolute difference between predicted and measured q''_{HFg}. Averaging was performed throughout the duration of experiments and over all measurement locations used for a given material. PMMA$_{EXT}$ data were not included in the evaluation because they were already utilized in the flame model parametrization. PMMA$_{CAST}$ data were included because this material was substantially different from PMMA$_{EXT}$ in terms of the melt flow and flame base movement.

As indicated by the data in Table 5, Method 1 was found to provide the most accurate predictions of flame heat flux. The predictions obtained with this method were, on average, within 3.8 ± 1.6 kW m^{-2} of the experimental data (here, this uncertainty

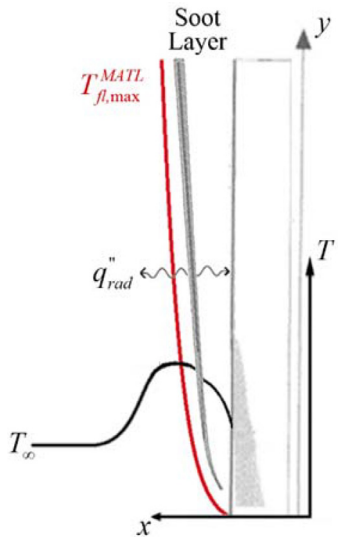

Fig. 22. A depiction of a laminar soot-producing diffusion flame on a sample surface.

represents two standard deviations of the mean; it indicates by how much the average error of model predictions differs between each material tested). To place this level of agreement in context, one may consider that the differences between flame heat flux measurements reported in the literature for similarly sized wall flames on the same material (e.g. PMMA) can be as high as 20 kW m^{-2} [43].

Figure 21 provides a detailed, time-resolved comparison between the experimental flame heat flux data and those predicted using Method 1 parameters. Note that in this figure, ABS and HIPS unshielded experimental measurements are only shown prior to significant soot deposition on the gauge. The worst agreement is observed for POM. The model underpredicts the peak, steady heat fluxes by 10–14 kW m^{-2} and, as indicated by the data in Table 5, none of the other explored heat of combustion definitions substantially improve this agreement. This discrepancy may be associated with a change in flame (to material surface) standoff distance, which would impact the value of the heat transfer coefficient (h_{flame}). However, an analysis of flame standoff distance based on comparison of a series of high resolution images taken from the sides of both POM and PMMA$_{EXT}$ flames of several heights did not reveal any significant differences in this parameter.

An alternative explanation for this discrepancy is associated with the soot-free nature of POM flames, as evidenced by their nearly uniform faint blue color (see Fig. 7). It is speculated that the soot layer present in the flames produced by all other materials examined in this study may act as a heat sink diverting a portion of the energy conducted toward the sample surface. The absence of a soot layer in POM flames thus leads to a higher flame heat flux to the surface. This speculation is illustrated by a depiction of the primary features of sooting flames in Fig. 22. It is shown that a portion of the energy conducted from the region of the flame with the highest temperature (designated by $T_{fl,\max}^{MATL}$) to the sample's surface is converted to radiation in the soot layer. Half of this converted energy (designated by q''_{rad}) is radiated toward the sample's surface; the other half is radiated away. While flame to surface heat transfer is believed to be dominated by convection for all studied materials, q''_{rad} may be sufficiently large (10–20% of q''_{HFg} as suggested by earlier measurements [18]) to be responsible for the observed discrepancies between the current flame model and POM data.

6. Conclusions

In this work, detailed measurements of sample mass loss rate and flame heat flux were obtained as a flame spread vertically upward over the surface of seven polymeric materials – ABS, HIPS, PBT, PMMA, POM, PP and UP – two of which are glass-reinforced composites. These materials are widely used in household goods, transportation vehicles and packaging applications and, collectively, they represent diverse fuel chemistry and a wide range of burning behaviors including polymer melt flow, sample burnout and heavy soot formation. Using these results, a previously developed empirical model, which calculates the complete heat feedback profile of a 3–20 cm tall buoyant diffusion flame on a vertically oriented PMMA surface from this material's width-normalized mass loss rate, was generalized to other pyrolyzable solids.

The generalized model requires knowledge of the heat of complete combustion of the gaseous pyrolyzates of the material of interest, which can be measured with a microscale combustion calorimeter, and the atomic composition of these pyrolyzates. The model yields an analytical relationship between width-normalized mass loss rate and spatially resolved flame heat feedback to the burning surface. This model was found to predict flame heat flux to a water-cooled gauge embedded into a material's surface with an average accuracy of ±3.8 kW m^{-2} (approximately 10–15% of peak flame heat flux).

As demonstrated in an earlier study [17], a combination of this flame model with a numerical pyrolysis solver produces a robust tool for the analysis of flame spread dynamics. This tool has a substantial limitation with respect to computational fluid dynamics based methods – it is only applicable to a specific problem geometry and gaseous flow conditions realized in a terrestrial environment. However, as discussed in Section 1, this geometry encompasses a wide range of important fire scenarios and, in terms of computational efficiency and accuracy, this tool is likely to be superior to any other existing models.

Acknowledgments

The authors would like to thank the Federal Aviation Administration for supporting this project under the Grant number 09-G-018, monitored by Dr. Richard E. Lyon.

Supplementary materials

Supplementary material associated with this article can be found, in the online version, at doi:10.1016/j.combustflame.2017.02.007.

References

[1] R.C. Thompson, C.J. Moore, F.S. Vom Saal, S.H. Swan, Plastics, the environment, and human health: current consensus and future trends, Philos. Trans. R. Soc. 364 (2009) 2153–2166.
[2] S. Kerber, Analysis of changing residential fire dynamics and its implications on firefighter operational timeframes, Fire Technol. 48 (2012) 865–891.
[3] ASTM International, ASTM Standard 1354-15A: standard test method for heat and visible smoke release rates for materials and products using an oxygen consumption calorimeter, ASTM International, West Conshohocken, PA, 2003 www.astm.org, doi:10.1520/E1354-15A.
[4] ASTM International, ASTM Standard E162-15A: standard test method for surface flammability of materials using a radiant heat energy source, ASTM International, West Conshohocken, PA, 2003 www.astm.org, doi:10.1520/E0162-15A.
[5] Underwriter's Laboratories, UL Standard 94: standard for safety of flammability of plastic materials for parts in devices and applications testing, Underwriter's Laboratories, Northbrook, IL, 2013 http://ulstandards.ul.com/standard/?id=94_6.
[6] Underwriter's Laboratories, UL Standard 1694: standard for tests of flammability of small polymeric component materials, Underwriter's Laboratories, Northbrook, IL, 2002 http://ulstandards.ul.com/standard/?id=1694.

[7] G. Grant, D. Drysdale, Numerical modelling of early flame spread in warehouse fires, Fire Saf. J. 24 (1995) 247–278.
[8] J. Quintiere, The application of flame spread theory to predict material performance, J. Res. Natl. Bur. Stand. 93 (1988) 61–70.
[9] A. Ito, T. Kashiwagi, Characterization of flame spread over PMMA using holographic interferometry sample orientation effects, Combust. Flame 71 (1988) 189–204.
[10] J. DeRis, Spread of a laminar diffusion flame, Symp. (Int.) Combust. 12 (1969) 241–252.
[11] F.A. Williams, Mechanisms of fire spread, Symp. (Int.) Combust. 16 (1977) 1281–1294.
[12] K. Saito, J.G. Quintiere, F.A. Williams, Upward turbulent flame spread, Fire Saf. Sci. 1 (1985) 75–86.
[13] M.M. Delichatsios, M.K Matthews, M.A. Delichatsios, An upward fire spread and growth simulation, Fire Saf. Sci. 3 (1991) 207–216.
[14] S.I. Stoliarov, I.T. Leventon, R.E. Lyon, Two-dimensional model of burning for pyrolyzable solids, Fire Mater. 38 (2013) 391–408.
[15] C. Lautenberger, A.C. Fernandeze-Pello, Generalized pyrolysis model for combustible solids, Fire Saf. J. 44 (2009) 819–839.
[16] K. McGrattan, S. Hostikka, J. Floyd, H. Baum, R. Rehm, Fire dynamics simulator (version 5) technical reference guide. NIST Special Publication 1018-5, NIST, 2007.
[17] I.T. Leventon, J. Li, S.I. Stoliarov, A flame spread simulation based on a comprehensive solid pyrolysis model coupled with a detailed empirical flame structure representation, Combust. Flame 162 (2015) 3884–3895.
[18] I.T. Leventon, Prediction of upward flame spread over polymers (Ph.D. dissertation), Department of Fire Protection Engineering, University of Maryland, 2016.
[19] A.C. Fernandez-Pello, T. Hirano, Controlling mechanisms of flame spread, Combust. Sci. Technol. 32 (1983) 1–31.
[20] K.C. Tsai, D. Drysdale, Flame height correlation and upward flame spread modelling, Fire Mater. 26 (2002) 279–287.
[21] M.A. Delichatsios, Flame heights in turbulent wall fires with significant flame radiation, Combust. Sci. Technol. 39 (1984) 195–214.
[22] A. Tewarson, D. Ogden, Fire behavior of polymethymethacrylate, Combust. Flame 89 (1992) 237–259.
[23] J.G. Quintiere, M. Harkleroad, Y. Hasemi, Wall flames and implications for upward flame spread, Combust. Sci. Technol. 48 (1986) 191–222.
[24] M.J. Gollner, F.A. Williams, A.S. Rangwala, Upward flame spread over corrugated cardboard, Combust. Flame 158 (2011) 1404–1412.
[25] T. Ahmad, G.M. Faeth, An investigation of the laminar overfire region along upright surfaces, J. Heat Transf. 100 (1978) 112–119.
[26] G.A. Marxman, Combustion in the turbulent boundary layer on a vaporizing surface, Symp. (Int.) Combust. 10 (1965) 1337–1349.
[27] I.T. Leventon, S.I. Stoliarov, Evolution of flame to surface heat flux during upward flame spread on poly(methyl methacrylate), Proc. Combust. Inst. 34 (2013) 2523–2530.
[28] K.C. Smyth, J.H. Miller, R.C. Dorfman, W.G. Mallard, R.J. Santoro, Soot inception on a methane/air diffusion flame as characterized by detailed species profiles, Combust. Flame 62 (1985) 157–181.
[29] G.E. Martin, Pyrolysis of reinforced polymer composites: parameterizing a model for multiple compositions (Master's thesis), Department of Fire Protection Engineering, University of Maryland, 2015.
[30] Worksafe Australia, National industrial chemicals notifications and assessment scheme: M390B unsaturated polyester resin, Full Public Report NA/166, Worksafe Australia, Sydney, Australia, Jul. 1994.
[31] ASTM International, ASTM Standard D7309-13: standard test method for determining flammability characteristics of plastics and other solid materials using microscale combustion calorimetry, ASTM International, West Conshohocken, PA, 2003 www.astm.org, doi:10.1520/D7309-13.
[32] R.E. Lyon, R.N. Walters, S.I. Stoliarov, N. Safronava, Principles and practice of microscale combustion calorimetry, FAA Report DOT/FAA/TC-12/53 R3, FAA, Apr. 2013.
[33] F. Raffan-Montoya, X. Ding, S.I. Stoliarov, R.H. Kraemer, Measurement of heat release in laminar diffusion flames fueled by controlled pyrolysis of milligram–sized solid samples: impact of bromine- and phosphorus-based flame retardants, Combust. Flame 162 (2015) 4660–4670.
[34] R.N. Walters, S.M. Hackett, R.E. Lyon, Heats of combustion of high temperature polymers, Fire Mater. 24 (2000) 245–252.
[35] J. Li, S.I. Stoliarov, Measurement of kinetics and thermodynamics of the thermal degradation for non-charring polymers, Combust. Flame 160 (2013) 1287–1297.
[36] K.T. Korver, A generalized model for wall flame heat flux during upward flame spread on polymers (Master's thesis), Department of Fire Protection Engineering, University of Maryland, 2015.
[37] K. Tu, J.G. Quintiere, Wall flame heights with external radiation, Fire Technol. 27 (1991) 195–203.
[38] National Institute of Standards and Technology, "NIST chemistry webbook," 2016, http://webbook.nist.gov/chemistry/ (Online, Cited 01.12.15).
[39] A. Tewarson, Generation of heat and chemical compounds in fires, in: P.J. DiNenno (Ed.), The SFPE Handbook of Fire Protection Engineering, 4th ed., National Fire Protection Association, Quincy, MA, 2008, pp. 3–109.
[40] A. Tewarson, J.L. Lee, R.F. Pion, The influence of oxygen concentration on fuel parameters for fire modeling, 18 (1981), pp. 563–570.
[41] A. Tewarson, Combustion efficiency and its radiative component, Fire Saf. J. 39 (2004) 131–141.
[42] J.G. Quintiere, R. Lyon, S. Crowley, An exercise in obtaining flame radiation fraction from the cone calorimeter, 14th International Conference and Exhibition on Fire and Materials (2015), pp. 149–161.
[43] Y. Pizzo, C. Lallemand, A. Kacem, A. Kaiss, J. Gerardin, Z. Acem, P. Boulet, B Porterie, Steady and transient pyrolysis of thick clear PMMA slabs, Combust. Flame 162 (2015) 226–236.